Journal of Energy Chemistry 94 (2024) 449–457

Contents lists available at ScienceDirect

Journal of Energy Chemistry

journal homepage: www.elsevier.com/locate/jechem

http://www.journals.elsevier.com/journal-of-energy-chemistry/

Regulating interfacial chemistry and kinetic behaviors of F/Mo co-doping Ni-rich layered oxide cathode for long-cycling lithium-ion batteries over −20 °C–60 °C

Siqi Guan [a,b], Lin Tao [a], Pei Tang [b,c], Ruopian Fang [e], Huize Wu [b,c], Nan Piao [b], Huicong Yang [b], Guangjian Hu [b,d,*], Xin Geng [a], Lixiang Li [a], Baigang An [a,*], Feng Li [b,c,d,*]

[a] Institute of Energy Materials and Electrochemistry Research, University of Science and Technology Liaoning, Anshan 114051, Liaoning, China
[b] Shenyang National Laboratory for Materials Science, Institute of Metal Research, Chinese Academy of Sciences, Shenyang 110016, Liaoning, China
[c] School of Materials Science and Engineering, University of Science and Technology of China, Shenyang 110016, Liaoning, China
[d] Shenyang King Power Tech. Co., Ltd., Shenyang 110016, Liaoning, China
[e] School of Chemical Engineering, The University of New South Wales, Sydney 2052, NSW, Australia

ARTICLE INFO

Article history:
Received 15 January 2024
Revised 24 February 2024
Accepted 25 February 2024
Available online 13 March 2024

Keywords:
Anion-cation co-doping
Wide temperature operation
Ni-rich layered cathode
Phase transition
Surface/interface

ABSTRACT

Ni-rich layered oxide cathodes have shown promise for high-energy lithium-ion batteries (LIBs) but are usually limited to mild environments because of their rapid performance degradation under extreme temperature conditions (below 0 °C and above 50 °C). Here, we report the design of F/Mo co-doped $LiNi_{0.8}Co_{0.1}Mn_{0.1}O_2$ (FMNCM) cathode for high-performance LIBs from −20 to 60 °C. F^- doping with high electronegativity into the cathode surface is found to enhance the stability of surface lattice structure and protect the interface from side reactions with the electrolyte by generating a LiF-rich surface layer. Concurrently, the Mo^{6+} doping suppresses phase transition, which blocks Li^+/Ni^{2+} mixing, and stabilizes lithium-ion diffusion pathway. Remarkably, the FMNCM cathode demonstrates excellent cycling stability at a high cutoff voltage of 4.4 V, even at 60 °C, maintaining 90.6% capacity retention at 3 C after 150 cycles. Additionally, at temperatures as low as −20 °C, it retains 77.1% of its room temperature capacity, achieving an impressive 97.5% capacity retention after 500 cycles. Such stable operation under wide temperatures has been further validated in practical Ah-level pouch-cells. This study sheds light on both fundamental mechanisms and practical implications for the design of advanced cathode materials for wide-temperature LIBs, presenting a promising path towards high-energy and long-cycling LIBs with temperature adaptability.

1. Introduction

Lithium ion batteries (LIBs) play a pivotal role in the development of electric vehicles, smart grids, and portable devices [1,2]. However, the majority of LIBs are limited to mild environments with a narrow temperature range. Operating at below 0 °C or above 50 °C often lead to degraded performance of LIBs and even battery failure, significantly limiting their potential applications across a wide temperature range. Cathode materials, as the active component in electrochemical reactions, exert a substantial influence on the wide temperature performance of LIBs. Notably, Ni-rich layered oxides, such as $LiNi_{0.8}Co_{0.1}Mn_{0.1}O_2$ (NCM811), have emerged as promising cathode materials for high-energy-density LIBs [3–5]. To facilitate the widespread use of LIBs across diverse temperatures, it is imperative to enhance the wide-temperature performance of Ni-rich layered oxides.

However, the stable operation of Ni-rich cathode materials faces persistent challenges due to their interfacial and structural instability [6,7]. During the lithiation/delithiation process, Ni^{2+} generated from the reduction of Ni^{3+}/Ni^{4+} migrates to octahedral vacancies, leading to Li^+/Ni^{2+} mixing and phase transition [8–10]. This phenomenon results in the formation of an inactive rock-salt phase, which greatly impedes the Li transport kinetics, especially at low temperatures. Moreover, side reactions between

* Corresponding authors.
E-mail addresses: gjhu@imr.ac.cn (G. Hu), bgan@ustl.edu.cn (B. An), fli@imr.ac.cn (F. Li).

https://doi.org/10.1016/j.jechem.2024.02.064

the Ni-rich oxides and the electrolyte at the cathode/electrolyte interface leads to the formation of a thickened cathode electrolyte interface (CEI) and the migration of transition metal (TM) ions to the anode, resulting in corrosion of the anode and accumulation of heterogeneous solid electrolyte interphase (SEI) [11]. These interfacial side reactions get excerbated during high-temperature cycling, leading to rapid degradation in capacity and Coulombic efficiency [12].

Considerable efforts have been dedicated to achieving stable operation of Ni-rich layered oxide cathodes at low or high temperatures [13,14]. Typical strategies include ion-doping and surface modification, which are aimed at stabilizing the crystal structure and enhancing the interfacial stability of Ni-rich layered oxides [14–19]. For instance, a conductive polymer coating on the surface of $LiNi_{0.88}Co_{0.09}Mn_{0.03}O_2$ was reported to effectively accelerate interfacial Li^+ transport kinetics at −20 °C due to improved electronic/ionic conductivity, enabling a 69% capacity retention compared to that delivered at 25 °C [20]. By co-doping $LiNi_{0.88}Co_{0.09}Mn_{0.03}O_2$ with yttrium and Titanium (Y/Ti), a capacity retention of 82.6% was achieved after 200 cycles at 55 °C [21]. However, most of these reports are constrained to a relatively narrow temperature range, typically between 30 to 50 °C [13,22,23]. Meanwhile, the capacity contribution at low temperatures mostly falls below 70%, and the capacity retention is often under 90% over 150 cycles at high temperatures. Consequently, achieving stable performance of Ni-rich cathode materials across an extensive temperature range over 60 °C remains a critical challenge, which requires comprehensive consideration of the fundamental challenges present at both low and high temperatures.

Herein, we report the facile synthesis of cation/anion co-doped NCM811 cathode material (FMNCM) to enable stable cycle of LIBs in a wide temperature range of 80 °C (−20–60 °C). The F^- doping onto the cathode surface can enhance the stability of surface lattice structure by bonding the Ni–F bond and protect the interface against electrolye-induced side reactions by generating a protective LiF-rich layer, especially at high temperatures. Concurrently, Mo^{6+} as cation doping within the bulk phase and grain boundary leads to effectively impeding Li^+/Ni^{2+} mixing, phase transition and enlarged interlayer spacing, while simultaneously accelerating the Li^+ transport kinetics especially at low temperatures. Benefiting from the above advantages, the FMNCM exhibits remarkably improved cycling stability at a voltage window of 2.7–4.4 V at 60 °C even under fast charging and discharging up to 3 C. Under a low operatinng temperature down to −20 °C, 97.5% capacity retention can be retained after 500 cycles at 0.5 C (retains 77.1% of room temperature capacity). Moreover, these findings are further validated in practical graphite/FMNCM pouch-cells with stable operation across wide temperature.

2. Experimental

2.1. Materials synthesis

The spherical $Ni_{0.8}Co_{0.1}Mn_{0.1}(OH)_2$ precursors were synthesized utilizing the coprecipitation method, wherein stoichiometric amounts of $NiSO_4{\cdot}6H_2O$, $CoSO_4{\cdot}7H_2O$ and $MnSO_4{\cdot}H_2O$ were dissolved in deionized water to form a mixing salt solution, each concentration being 2 mol L^{-1}. As precipitation and chelating agents, NaOH (4 mol L^{-1}) and $NH_3{\cdot}H_2O$ (2.4 mol L^{-1}) were employed, respectively. The entire solution ensemble was introduced into a continuously stirred tank reactor maintained at 55 °C under a N_2 atmosphere. The precursors were ultimately obtained through a sequence involving filtration of the precipitate, thorough washing, and subsequent drying in a vacuum oven at 100 °C overnight. The precursors were thoroughly blended with $LiOH{\cdot}H_2O$ (Li: $Ni_{0.8}Co_{0.1}Mn_{0.1}(OH)_2$ ratio = 1.05:1) and calcined at 450 °C for 6 h followed by 750 °C for 15 h in an oxygen atmosphere. In the synthesis of FMNCM, the aforementioned precursors were combined with 1 mol% F (NH_4F) and 1 mol% Mo ($(NH_4)_6Mo_7O_{24}{\cdot}4H_2O$), undergoing a similar calcination process. For comparative purposes, pristine and F or/and Mo-doped NCM811 samples were fabricated utilizing a comparable methode.

2.2. Materials characterizations

The elemental compositions were meticulously analyzed using inductively coupled plasma-optical emission spectrometry (ICP-OES) on a Thermo Fisheries iCAP 7400 instrument. X-ray diffraction (XRD) experiments were conducted utilizing a Bruker D8 Advance diffractometer, employing Cu K_α radiation with a wavelength (λ) of 1.5418 Å. The X-ray absorption spectra were collected on the easyXAFS300 +. X-ray absorption spectra were acquired using the easyXAFS300+, and subsequent data analysis was carried out using the Demeter program. Extracting extended X-ray absorption fine structure (EXAFS) oscillations involved subtracting atomic background through a cubic spline fit to k^3-weighted data, where k represents the photoelectron wave number. The resulting $\chi(k)$ functions underwent Fourier transformation into R-space, with the Fourier-transform window set in the k range of 2–10 $Å^{-1}$. For crystal structure analysis, the Rietveld refinement method was applied using GSAS software. In-situ XRD testing employed a specially equipped Swagelok cell. Morphology and microstructure assessments were conducted through scanning electron microscopy (SEM, FEI Verios 460) equipped with an energy dispersive spectrometer (EDS), transmission electron microscopy (TEM, Tecnai F20), and spherical aberration-corrected transmission electron microscopy (STEM, ACTEM, Spectra 300). X-ray photoelectron spectroscopy (XPS) measurements were carried out on an ESCALAB 250Xi instrument. For depth analysis, an Ar^+ beam (5 keV) was employed for sample etching. Time-of-flight secondary ion mass spectrometry (TOF-SIMS) spectra were collected using the ION-TOF 5 instrument, with a sputtering area on cycled electrodes measuring 300 μm × 300 μm.

2.3. Electrochemical measurements

For the construction of cathode electrodes, the synthesized active materials were homogeneously blended with KS-6 and poly(vinylidene fluoride) (in a mass ratio of 90: 5.5: 4.5) in N-methyl-1, 2-pyrrolidone (NMP). The slurry was evenly coated onto an aluminum foil current collector. The cathode electrodes were then fashioned into ϕ12 mm tablets with a mass loading of approximately 4 mg cm^{-2}. To comprehensively evaluate the electrochemical performance, half-cell tests were conducted using 2032 coin-type cells with lithium metal serving as the anode. Electrochemical capacity tests were performed between 2.7 and 4.4 V (vs. Li/Li^+) for coin-type half-cell (1.0 C = 180 mA h g^{-1}). In demonstrating the practical viability of FMNCM, pouch-type cells were assembled using a mixed slurry of active materials (94 wt %), KS-6 (3 wt%), and polyvinylidene fluoride (PVDF) (3 wt%). The anode comprised graphite (Shandong Tian'an Huali New Material Technology Co. LTD, with a median particle size of D50 = 13.6 μm), and the N/P ratio for each electrode fell within the range of 1.10–1.15 (cathode coating ~20.5 mg cm^{-2}). The pouch cells were assembled using a stacked process. All electrochemical tests throughout this investigation utilized a 1 M $LiPF_6$ electrolyte in ethyl carbonate/diethylene carbonate/ethyl methyl carbonate (EC: DEC: EMC = 3: 2: 5 by volume%) with the addition of a 2 wt % lithium difluoro(oxalate) borate additive. Pouch-cell assessments were conducted at different temperatures (25 °C, −20 °C, and 60 °C) and within the same voltage windows (2.8 to 4.25 V). Cycle

stability under elevated cut-off voltage conditions was evaluated between 2.8 and 4.35 V at 25 °C. The electrochemical impedance spectroscopy (EIS) and cyclic voltammetry (CV) data were collected using a Bio-Logic EC-LAB SP-300 electrochemical workstation, with a frequency range of 10^5–0.01 Hz for EIS and a scan rate of 0.1 mV s^{-1} within the voltage range of 2.7 to 4.4 V for CV. Galvanostatic intermittent titration technique (GITT) measurements were conducted employing a 0.1 C rate for 15 min followed by a 30 min rest period, spanning the voltage range of 2.7–4.4 V.

2.4. Computational methods

Density functional theory (DFT) calculations were employed to attain structural relaxation and electronic energy within the Dmol3 module, utilizing the general gradient approximation (GGA) exchange–correlation functional. The Perdew-Burke-Ernzerhof (PBE) functional was specifically chosen for modeling these interactions. To account for long-range dispersive forces, the DFT-D approach with Grimme vdW correction was applied uniformly across all computations. A real-space global cutoff radius of 4.9 Å was implemented, and the Brillouin zone was systematically sampled through a 2 × 2 × 1 k-point grid using the Monkhorst-Pack scheme, ensuring the generation of high-quality calculation results. Structural optimizations were executed with stringent convergence criteria, set at 0.005 Å for maximum displacement, 1×10^{-5} eV for energy, and 0.01 eV $Å^{-1}$ for forces. A vacuum region of 20 Å was vertical to the surface to avoid the interaction between two periodic units.

3. Results and discussion

3.1. Theoretical calculation and physicochemical characterizations

To gain deeper insights into the intricate interplay between F^- and Mo^{6+} within NCM811, we employed DFT calculations to assess the relative energies associated with F and Mo doping at various layers, including the top surface and the first, second, and third Ni layers (Fig. 1a). For simplification purposes, $LiNiO_2$, exhibiting identical structural features to FMNCM derived from $LiNiO_2$, was chosen as a model for our calculations [24]. Fig. 1(b) reveals that F-doping on the internal TM layer is structurally unstable, leading to its inclination to migrate towards the surface. Simultaneously, Mo on the surface exhibits structural instability, showing a tendency to penetrate into the inner layers. This structural instability arises from the substantially larger radius of F^- compared to that of TM cations, while the radius of Mo^{6+} is close to those of TM cations. The outcomes of our DFT calculations unequivocally support the favorability of F/Mo co-doping into NCM811. Moreover, the wavelet transforms (WT) of the EXAFS signals provide additional confirmation of Mo diffusion into the bulk phase (Fig. 1c and d). A conspicuous shift in the peak of Mo to a higher wavenumber, as observed in the doped sample compared to the pristine one, serves as clear evidence of the incorporation of heavy atoms [25]. To delve into the impact of FMNCM structures, we calculated the charge difference. Fig. 1(e) illustrates the charge difference for a two demensional (2D) slice along the plane passing through the substituted Ni or the doped F/Mo. Notably, a substantial accumulation of electrons between the Ni near F and Mo atoms is evident, indicative of strengthened chemical bonds involving Mo–O and Ni–O. Furthermore, the Ni–O bond lengths for F/Mo doping are observed to be correspondingly shortened, providing valuable insights into the structural alterations induced by F/Mo co-doping in NCM811 (Fig. S1). To probe the nuanced changes in local electron structure due to F/Mo co-doping, Ni K-edge X-ray absorption near-edge structure (XANES) analyses were conducted on NCM811 and FMNCM samples (Fig. 1f).

Results reveal a higher Ni oxidation state in FMNCM, indicative of improved Ni^{3+}/Ni^{4+} redox utilization and reversibility [26]. Complementary EXAFS analysis demonstrates reduced Ni–O interatomic distances in FMNCM, aligning with simulation results (Fig. 1g). This reduction, facilitated by F/Mo co-doping, enhances electron storage capacity, reducing voltage hysteresis during charging and discharging. The process mitigates surface structural collapse and alleviates the H2 → H3 phase transition during cycling (Fig. S2) [25,27]. Based on the above analyses, we propose a one-step calcination method for the anion-cation co-doping of NCM811 cathode materials with F/Mo. Both NCM811 and FMNCM demonstrate a well-defined spherical morphology by SEM (Fig. S3). The FMNCM maintains smaller primary particles than the NCM811. Inductively coupled plasma (ICP) analysis confirmed the elemental composition of the obtained materials (Table S1), which are basically consistent with the designed chemometry. The XRD rietveld refinement results of the as-prepared samples are shown in Fig. 2(a and b) and Fig. S4. The results confirm that all samples show a typical α-$NaFeO_2$ hexagonal layered structure with R $\bar{3}$ m space group, and the crystal structure maintains with F/Mo co-doping [28]. In contrast to NCM811, the c lattice parameter of FMNCM experiences an increase from 14.157 to 14.220 Å (refer to Table S2). This expansion aligns with a subtle SEM (Fig. S3). This expansion aligns with a subtle enlargement in the Li-layer spacing, a phenomenon attributed to the lattice contraction within the $(Ni)O_6$ octahedron. F/Mo co-doping increases the local electron density and shortens the bond length of TM–O, leading to lattice contraction [29]. The slightly increased lattice parameters in FMNCM with widened c-spacing bring benefits to the transport of Li^+ in the bulk phase [30,31]. Besides, as shown in HAADF-STEM (Fig. 2c and d), NCM811 and FMNCM show layered structure, as identified via the corresponding fast Fourier transform. The layer spacing of FMNCM is increased by 0.2 Å, which corresponds to the increase of c lattice parameter. The altered primary particle exhibits a uniform distribution of Ni, Co, Mn, O, Mo, and F elements, as evidenced by EDS mapping. Notably, the elemental mapping of particle section shows that even at a doping amount of 1 mol%, the F dopants tend to be concentrated in the surface layer of FMNCM, while the Mo dopants show high concentrations at grain boundaries and throughout the primary particles (Fig. 2e). The substitution of oxygen sites by F in FMNCM decreases the cationic mixing by the compensate electrical neutrality. The presence of Mo can retard crystal boundary migration, thereby increasing the stablity of the crystal structure [30,32].

3.2. Electrochemical energy storage performance

To elucidate the impact of FMNCM on electrochemical performance, we present the differential capacity (dQ/dV) profiles of both NCM811 and FMNCM in Fig. 3(a). The dQ/dV curves manifest a series of phase transitions hexagonal to monoclinic (H1 → M), monoclinic to hexagonal (M → H2), hexagonal to hexagonal (H2 → H3) during lithiation, followed by the reverse sequence during delithiation [33]. Notably, the H2 → H3 phase transition, inducing strain along the *c*-axis, is delayed to higher voltage in FMNCM (ΔE = 27 mV). This delay significantly mitigates the phase transition, enhancing structural stability and reversibility. Additionally, the main characteristic of kinetic hindrance is the suppression of the dQ/dV peak intensity at approximately 3.5 V during discharge [34,35]. The kinetic hindrance of NCM811 has been effective relieved for F/Mo co-doping. Despite the similar initial discharge capacities (Fig. S5a), FMNCM exhibits obviously enhanced cycle life and rate capability compared to NCM811. At the rate of 5.0 C, the

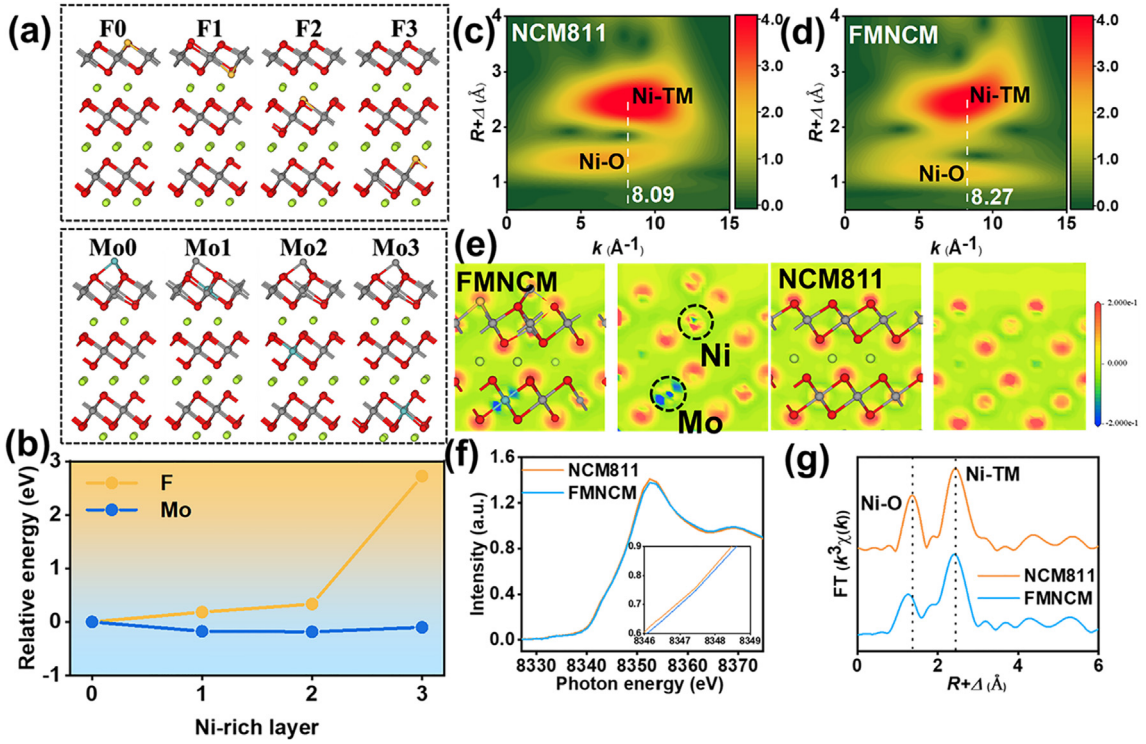

Fig. 1. Calculation of F/Mo dual modification. Doping (a) F and Mo introduced to the surface, 1st, 2nd, and 3rd layer, respectively. Ni, Li, F, O, and Mo atoms are denoted by gray, light-green, khaki, red, and cyan balls, respectively. (b) The F/Mo migration energy difference from the surface to the third layer. (c, d) EXAFS WT images of the NCM811 and FMNCM samples. (e) The charge difference for a slice through the substituted F/Mo, (f) XANES spectra of Ni K-edge, Insets: XANES spectra in the range of 8346–8349 eV and (g) EXAFS K space curves of NCM811 and FMNCM samples.

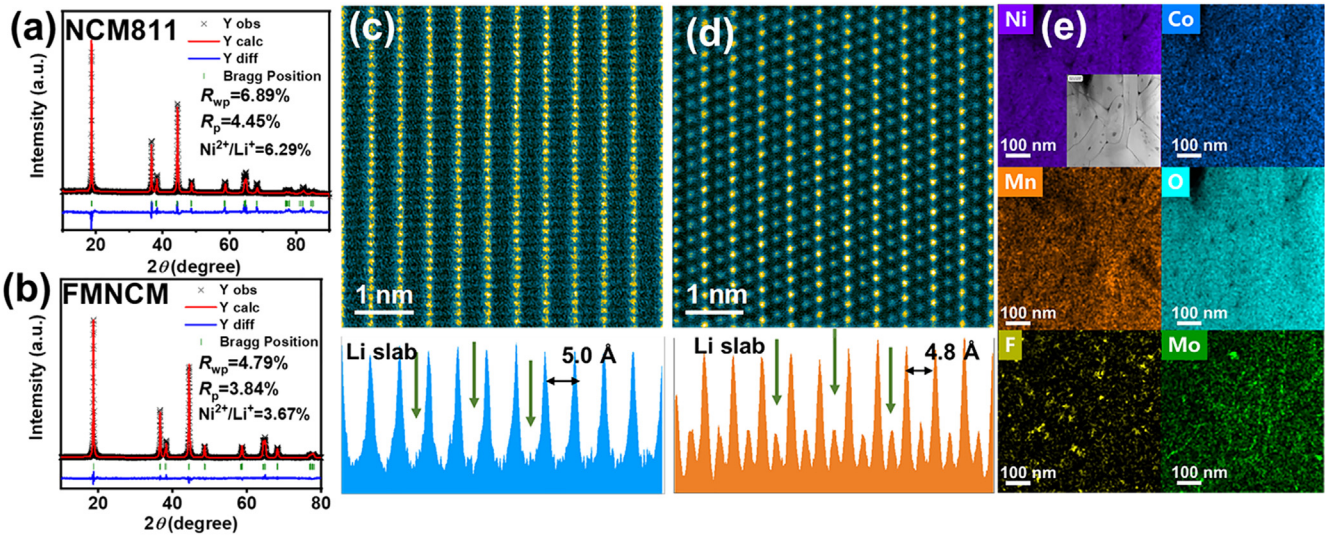

Fig. 2. Rietveld refinements of X-ray diffraction pattern for (a) NCM811 and (b) FMNCM, HAADF-STEM and corresponding HAADF simulation images of (c) FMNCM and (d) NCM811, (e) elemental mapping of the FMNCM.

FMNCM cell exhibits a notable reversible discharge capacity of 161.7 mA h g^{-1}, equivalent to 81.9% of the capacity observed at 0.2 C, surpassing its NCM811 (118.7 mA h g^{-1}) counterpart (Fig. 3b). Impressively, as the rate reverts to 0.5 C, the FMNCM cell demonstrates almost complete capacity recovery. The superior rate capability of the FMNCM cathode can be ascribed to the increase and stabilization of Li-layer spacing that contributes to enhanced ion diffusion, particularly under high rates. At 5.0 C, the discharge capacity of NCM811 experiences rapid degradation, with only 97.9 mA h g^{-1} retained after 200 cycles. While the discharge capacity of FMNCM remains at 151.7 mA h g^{-1} under the same conditions (Fig. S5b and c). At room temperature (25 °C), the FMNCM cell maintains a high discharge capacity of 157.8 mA h g^{-1} at 1.0 C, with a cut-off voltage of 4.4 V after 500 cycles surpassing the performance of the NCM811 cell (122.6 mA h g^{-1}) (Fig. 3c). Moreover, the pouch-cell with the FMNCM cathode displays a long cycle life with capacity retention rates of ~81.4% over 750 cycles at 1.0 C (Fig. 3d) and ~80.5% over 350 cycles at 0.5 C (Fig. S5d).

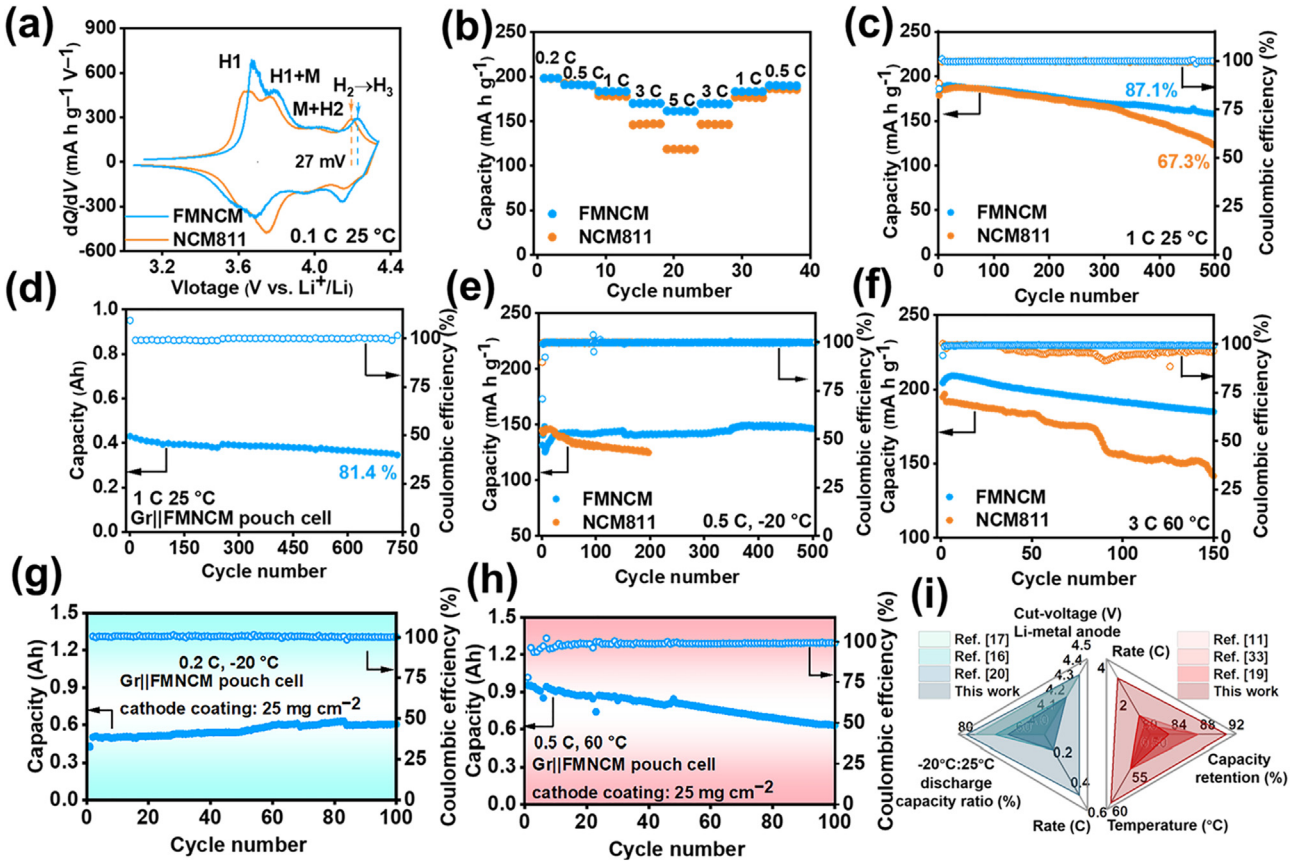

Fig. 3. Electrochemical characterizations of coin-type half-cell within the voltage range of 2.7–4.4 V. (a) The d*Q*/d*V* curves of NCM811 and FMNCM, (b) rate performance of NCM811 and FMNCM. Cycling stability for NCM811 and FMNCM at (c) 25 °C, (d) −20 °C (e) 60 °C. Pouch-type all-cell cycling stability of FMNCM as cathode and graphite as anode within the voltage range of 2.8–4.25 V at (f) 25 °C, (g) −20 °C, (h) 60 °C. (i) Comparison of the operational temperature range for rich-Ni NCM cathode materials.

The above discussions collectively highlight the superior electrochemical performance exhibited by the FMNCM electrode material in comparison to NCM811. This enhancement can be attributed to the effective inhibition of phase transitions and the mitigation of interfacial side reactions [36,37]. Nevertheless, FMNCM with superior structural stability is capable of stable operation across a broad temperature range. The capacity of FMNCM cell at −20 °C is 145.1 mA h g^{-1} after 500 cycles at 0.5 C (97.5% of the capacity retention) (Fig. 3e), higher than that for the NCM811 cell (124.3 mA h g^{-1}, 85.5% of capacity retention after 200 cycles). We further evaluated the structural and thermal stability of the cathode charged to 4.4 V through differential scanning calorimetry (DSC) profiles. FMNCM exhibits an exothermal peak at 228.1 °C with a heat generation of 36.4 J g^{-1}. In comparison, NCM811 shows a lower temperature peak (220.7 °C) with a higher overall heat generation of 69.8 J g^{-1} (Fig. S6). Even at a high temperature of 60 °C, FMNCM demonstrates outstanding cycling stability at 3 C. As shown in Fig. 3(f), the capacity of the NCM811 cell drops from 191.7 to 136.9 mA h g^{-1} after 150 cycles, while the FMNCM cell maintains a stable capacity of 184.7 mA h g^{-1}. Notably, the Coulombic efficiency of the FMNCM cell maintains around 99.5%, while the NCM811 cell experiences obvious degradation in CE after 30 cycles, signifying material structure degradation. To further evaluate the effectiveness of FMNCM for practical applications, pouch-cells with FMNCM cathodes and commercial graphite anodes were assembled and tested. As shown in Fig. 3(g), the pouch-cell shows an increasing trend over 100 cycles at −20 °C. The initial capacity rise is attributed to the activation stage, and the subsequent capacity increase may stem from lithium replenishment during the reactivation process within the graphite anode. When the temperature is elevated to 60 °C, the pouch cell retains 75% capacity over 100 cycles (Fig. 3h). Comparatively, the FMNCM cathodes exhibit excellent performance across a wide temperature range, as summarized in Fig. 3(i) and Tables S3, S4 [38]. These results indicate that, the F/Mo co-doping significantly enhances the structural and interface stability of the FMNCM cathode, resulting in exceptional performance across a broad temperature range.

3.3. Structural evolution and surface analysis

For an in-depth exploration of the structural phase transitions during the lithiation/delithiation process in NCM811 and FMNCM, in-situ XRD analyses were conducted on cells cycled at 0.1 C within the voltage range of 3.0–4.4 V. Throughout the cycling of NCM811 and FMNCM cathodes, the presence of peaks (003), (101), (006), (102), (104), and (105) indicates a consistently high crystallinity in the layered hexagonal phase structure (Fig. S8). Upon charging to around 4.0 V, the (003) reflection of NCM811 shifts negatively, suggesting gradual Li^+ deintercalation along the *c*-axis and an incremental expansion of the crystal structure, indicative of a phase transformation from H1 to M. Further charging to 4.4 V results in a pronounced shift of the (003) diffraction peak to higher 2θ values, signifying a significant lattice contraction along the *c*-axis during the irreversible H2 → H3 phase transition [39]. In contrast, FMNCM exhibits a more confined shift in the (003) peak at a high cut-off voltage of 4.4 V, displaying reversible structural evolution (Fig. 4a). This indicates that F/Mo co-doping effectively mitigates structural collapse, suppresses two-phase separation, and enhances the reversibility of the H2 → H3 phase transition in NCM811. The shift in the (003) diffraction peak, coupled with

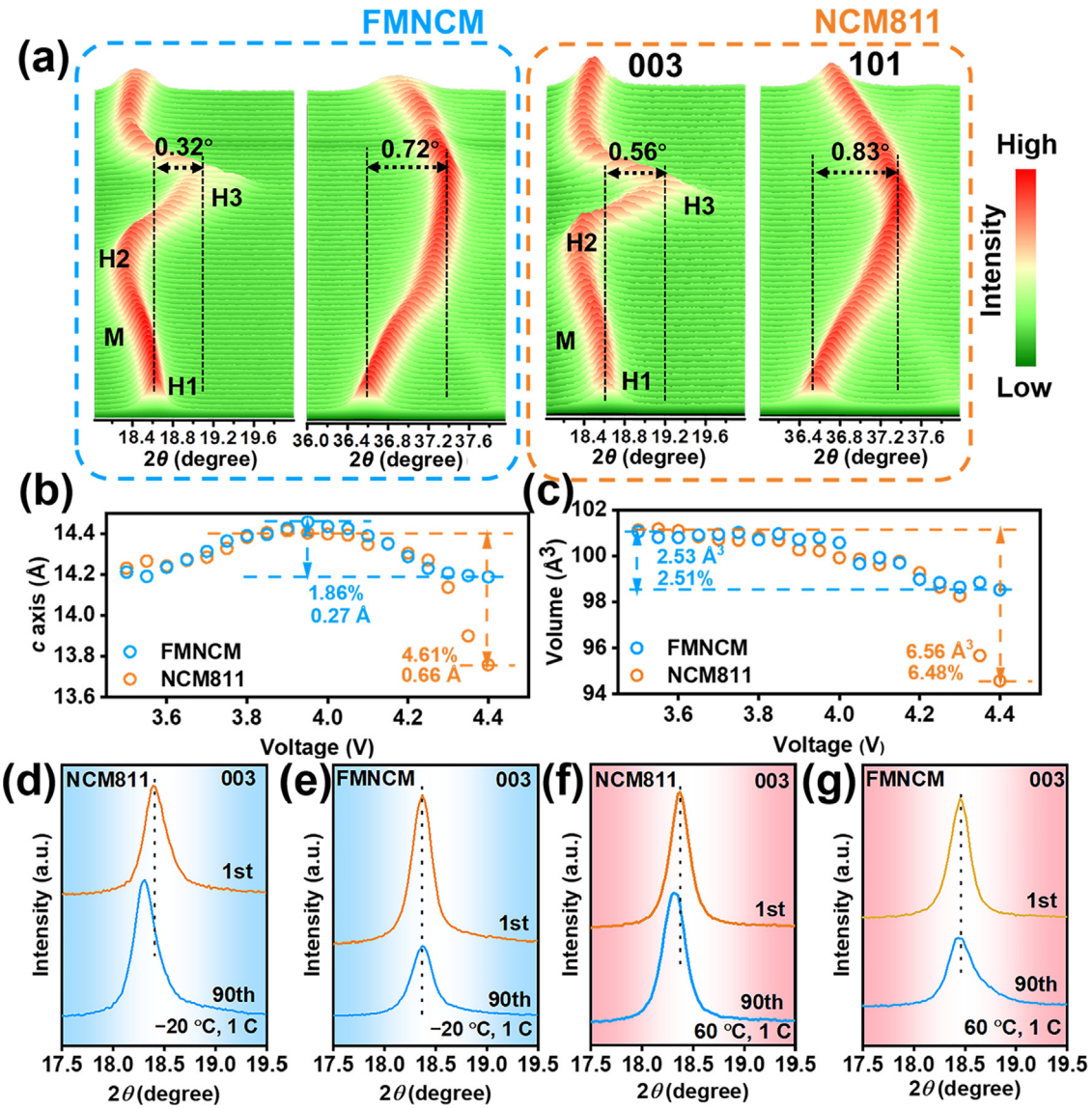

Fig. 4. (a) In-situ XRD characterizations of FMNCM and NCM811 during the initial charge–discharge cycle at 25 °C. Lattice parameters of *c* axis (b) and volume (c) as functions of voltage at different cutoff voltages, ex-situ XRD patterns of the NCM811 (d, f) and FMNCM (e, g) electrodes after various cycles at −20 and 60 °C.

the alteration of the inter-slab distance, signifies changes in the voltage state. During the charging stage at 4.4 V, NCM811 undergoes significant changes in lattice parameter *c* (0.66 Å or 4.61%) and volume (6.56 Å^3 or 6.48%) (Fig. 4b). In comparison, FMNCM exhibits substantially smaller changes in both lattice parameters (1.86% and 2.51%, respectively) during the same stage (Fig. 4c). This reduced lattice contraction in FMNCM is attributed to the stabilizing effect of compatible F/Mo co-doping, effectively minimizing TM ions migration and maintaining local structural integrity [40]. Mo-doping individually exhibited a mitigating effect on structure phase transitions, further emphasizing the significance of Mo elements in stabilizing the bulk phase structure (Fig. S9). Ex-situ XRD tests on NCM811 and FMNCM electrodes after different cycles at −20 and 60 °C (Fig. 4d–g) confirm that the crystal structure remains similar to the first cycle. The (003) reflection peaks of FMNCM cathodes maintain their position after various cycles at −20 and 60 °C, confirming that the crystal structure remains similar to the first cycle. The (003) reflection peaks of FMNCM cathodes maintain their position after various cycles at −20 and 60 °C, ensuring stable Li^+ pathways and facilitating efficient charge extraction. By contrast, NCM811 cathodes exhibit noticeable shifts in the (003) reflection peaks with increased cycles, indicating that the FMNCM strategy restrains significant lattice structural changes and enhances the integrity of the layered structure. Confirm that the crystal structure remains similar to the first cycle. The (003) reflection peaks of FMNCM cathodes maintain their position after various cycles at −20 and 60 °C, ensuring stable Li^+ pathways and facilitating efficient charge extraction. By contrast, NCM811 cathodes exhibit noticeable shifts in the (003) reflection peaks with increased cycles, indicating that the FMNCM strategy restrains significant lattice structural changes and enhances the integrity of the layered structure.

Establishing a stable and robust interface layer in electrodes is crucial for achieving good cycling performance of Ni-rich NCM cathodes [41,42]. To validate the improvements brought about by F/Mo co-doping, cycled cells were disassembled, and the chemical compositions of the outer CEI and SEI from the harvested cathodes and anodes were investigated. Time-of-flight secondary ions mass spectrometry (TOF-SIMS) depth profiles of cycled electrodes indicate that the CEI films consist of the outer and inner layers. As

shown in Fig. 5 (a), a 3D render illustrates the concentration gradient of LiF^-, with the LiF-enriched surface of FMNCM serving effectively as an interfacial passivation layer to mitigate excessive electrolyte oxidation [43]. Chemical-depth profiles (Fig. 5b) reveal multicomponents within the CEI film, with species like C_2F^-, PO_3^-, and NiF_3^- mainly originating from electrolyte decomposition [18]. Notably, the amounts of these species in the FMNCM cathode CEI film are lower than those in NCM811, indicating the superior stability of FMNCM under high-voltage cycling conditions. For the SEI, the Ni^- species in the SEI film of FMNCM are lower than those in NCM811 at various temperatures (Figs. S10–S12), as further validated by 3D visualization (Fig. 5c). XPS analysis was also performed to investigate the chemical compositions of the SEI on the extensively cycled Li anodes. High-resolution F 1*s* spectra and XPS depth analysis of Ni 2*p*, O 1*s*, and F 1*s* on extensively cycled Li anodes further emphasize the advantages of F/Mo co-doping. The Ni content in the Li anode of FMNCM is notably decreased, indicating that F/Mo co-doping enhances the energy of Ni–O bonds, reducing TMs dissolution and improving the stability and reversibility of the interface layer (Fig. S13a–c). The Li anodes after 500 cycles were also analyzed by ICP to test the content of Ni element, which derives from its dissolution during cycling (Fig. S13d). In high-resolution F 1*s* spectra (Fig. S14a and b), LiF peak at 684.8 eV is observed in both samples during the initial scan. With Ar^+ etching for 300, 450, and 600 s, the Li_xPOF_y peak of NCM811 anode SEI film appeares. The high-resolution O 1*s* XPS spectra of the SEI show the presence of Li_2O (529.1 eV) and C=O/$ROCO_2Li$ (531.3 eV) (Fig. S14c and d) [44]. With increasing Ar^+ etching time, the contents of Li_2CO_3/$ROCO_2Li$ increase in the SEI of the anode for the cell with NCM811, whereas it remains unchanged on SEI film of the FMNCM anode. SEM images of electrodes cycled for 200 cycles (Fig. 5d) reveal that the Li-plate surface of NCM811 exhibits a fibrous and porous morphology with serious Li dendrites, indicative of dendritic growth and electrolyte consumption [45,46]. In contrast, the Li-plate surface of FMNCM is dense and smooth, suggesting a stable and reversible SEI. This outcome aligns with the widely recognized need to enhance homogeneous Li deposition to suppress dendritic plating on the anode surface [47]. Digital photos of the cathode and anode electrodes after the cycles also confirm this concept (Fig. S15). Collectively, these results demonstrate that the F/Mo co-doping improved stability of the interfacial coordination environment, reducing the migration of transition metals.

3.4. Structural stability and schematic diagram

To delve into the mechanism of capacity fading in NCM811 and elucidate the benefits of F/Mo co-doping, the morphological and crystal structure evolutions after 150 cycles were investigated through cross-sectional Transmission Electron Microscopy (TEM) and Scanning Transmission Electron Microscopy (STEM). As shown in Fig. 6(a), evident intergranular cracks and nanopores are observed within NCM811 particles, leading to distorted pathway for electrons and Li^+ and impeded charge transfer through the voids. The STEM image reveals an unstable rock-salt phase structure with a thickness of approximately ~4.5 nm on the outer surface of NCM811, indicating pronounced interfacial reactions and irreversible phase transitions (Fig. 6b) [16]. The accumulation of surface phase transitions in NCM811 during cycling at the high cut-off voltage of 4.4 V is primarily attributed to electrolyte erosion and uneven Li^+ transport [48]. In contrast, FMNCM exhibits a compact cross-profile without voids, retaining its mechanical integrity (Fig. 6c and d). The bulk of FMNCM maintains its original layered structure (R $\bar{3}$ m) with a thin rock-salt phase of ~1.9 nm on the particle surface (Fig. 6e), which indicates good interfacial stability of FMNCM. The surface phase transition of the only Mo-doping electrode was observed to be 2.2 nm, which is lower than that of the NMC811 (Fig. S16). The EIS patterns of cycled electrodes (Fig. 6e and f) demonstrate a much lower impedance increase for FMNCM compared to NCM811 over different cycles, indicating the formation of a stable interface layer during the initial cycles [49]. All impedance spectra were fitted with an equivalent circuit to determine the values of R_s, R_f, and R_{ct}. The results are listed in Table S5. Furthermore, the analysis of galvanostatic intermittent titration technique reveals that the FMNCM cell exhibits double the value of lithium ion mobility (D_{Li}^+) with a measurement of $10^{-8.7}$ cm^2 s^{-1}, as compared to the NCM811 cell with $10^{-9.1}$ cm^2 s^{-1} (Fig. S17). Overall, the current study suggests that FMNCM exhibits enhanced bulk phase kinetics at low temperatures (−20 °C) and

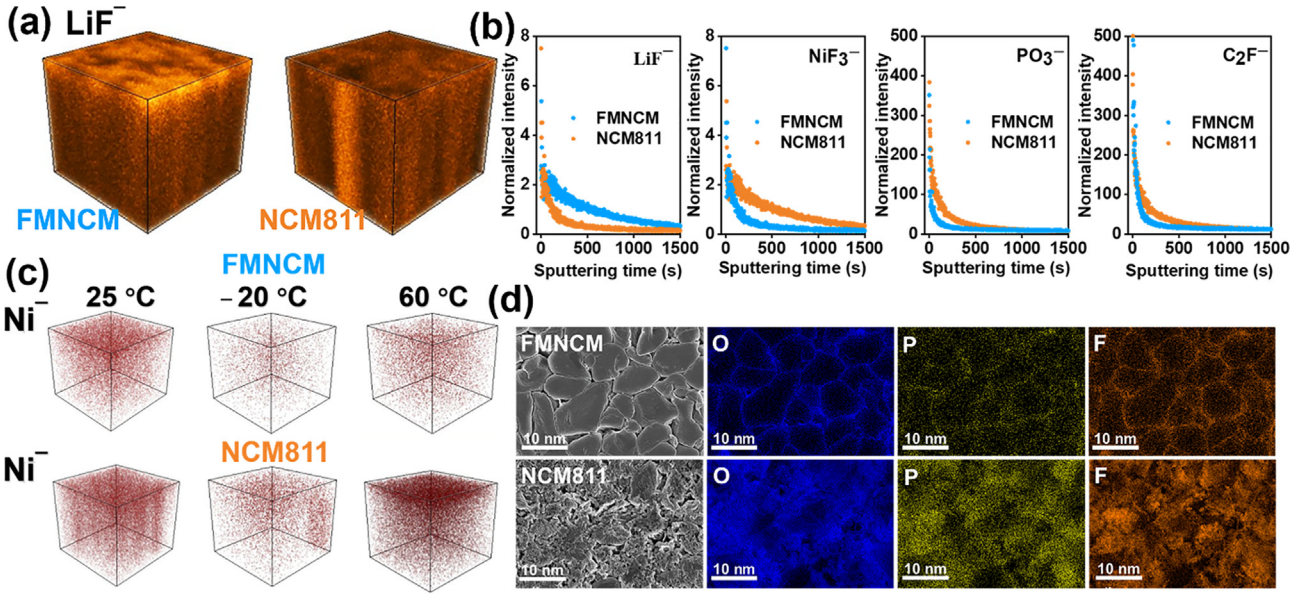

Fig. 5. Ex-situ TOF-SIMS depth profiles of cathode electrodes (a) 3D render of composition (LiF^-). (b) Chemical characterizations of cathode surface. (c) 3D render and concentration distribution of anode electrodes (FMNCM and NCM811 counter electrodes). Note: 25 °C (after 200 cycles), −20 °C (after 100 cycles) and 60 °C (after 100 cycles). (d) SEM images and EDS maps of anode electrodes after 200 cycles at 25 °C.

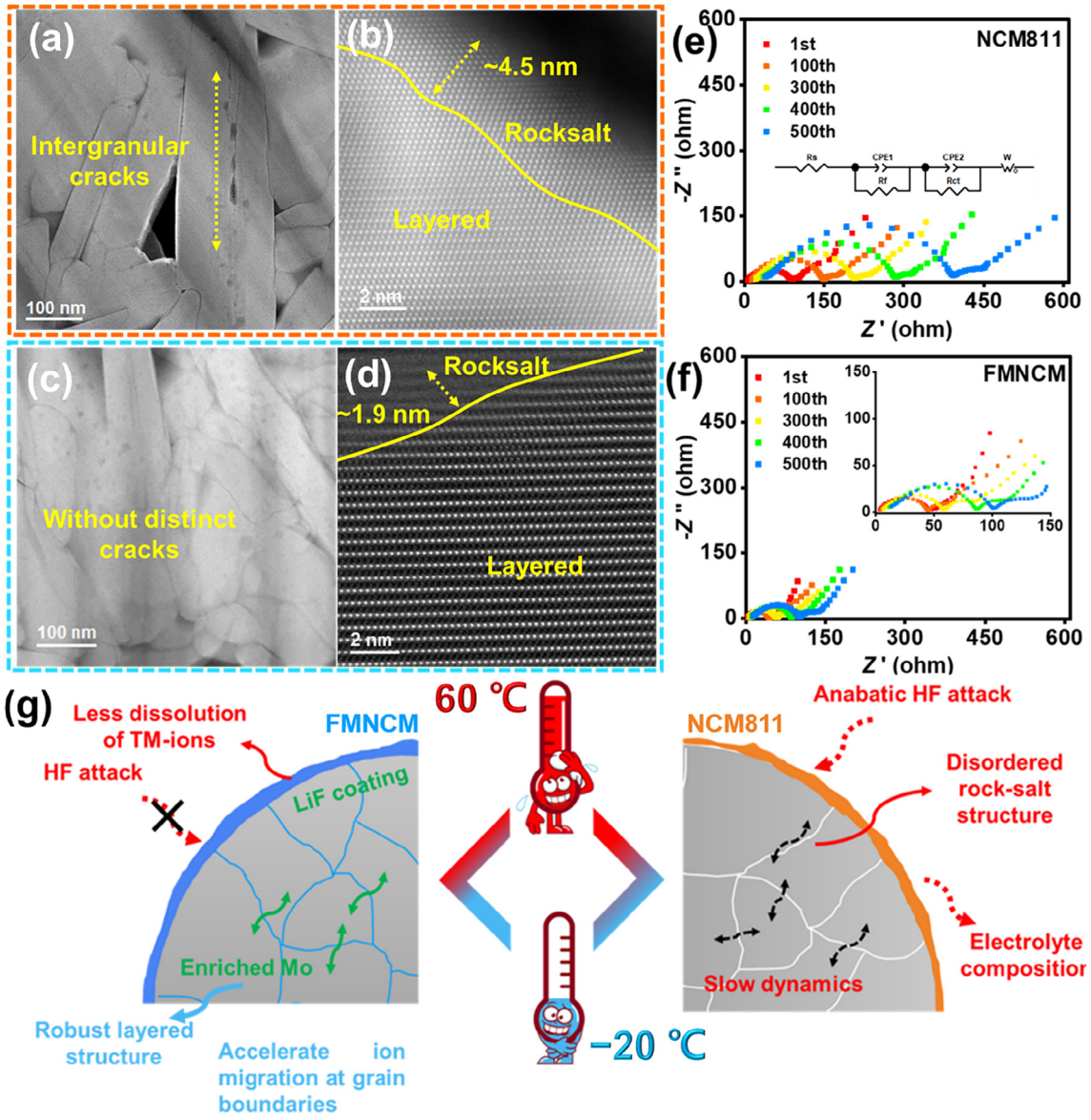

Fig. 6. Morphology and crystal structure of NCM811 and FMNCM after 150 cycles at 1 C within 2.7–4.4 V. Cross-sectional TEM and corresponding HAADF-STEM images of particle surface of interior region for FIB-prepared (a, b) FMNCM, (c, d) NCM811. Nyquist plots of NCM811 (e) and FMNCM (f) cathodes at fully charged state after different cycling numbers. (g) Schematic illustration of deterioration evolution for NCM811 and FMNCM electrodes during cycling.

improved interfacial thermodynamic stability at elevated temperatures (60 °C) (Fig. 6g), emphasizing the potential of FMNCM as a promising cathode material for LIBs intended for use across a broad temperature range.

4. Conclusions

In summary, we present the design of a F/Mo co-doped Ni-rich layered oxide cathode for LIBs with excellent performance over a wide temperature range of 80 °C. DFT calculations and electrochemical tests reveal that the incorporation of F/Mo enhances the stability of Ni and O in the crystal structure, allowing for an extended operating temperature range. The prominent role of Mo^{6+} doping in NCM811 is identified, enhancing Li^{+} migration rates and reducing lattice contraction at long cycles, thereby improving reaction kinetics even at low temperatures (−20 °C). Simultaneously, the F^{-} on the surface layer of NCM811 reinforces the stability of the interfacial metal coordination, mitigating the dissolution of transition metal cations and side reactions with the electrolyte at elevated temperatures (60 °C). Consequently, the pouch-cell utilizing the dual-doped cathode material demonstrates superior reversibility, achieving 81.4% capacity retention over 750 cycles at 25 °C. Remarkably, it exhibits outstanding cycling performance across a wide temperature range, maintaining stable operation at both −20 °C and 60 °C. This study provides a valuable insight into overcoming barriers associated with wide-temperature applications of Ni-rich layer materials via elemental co-doping, presenting a promising avenue towards high-energy and long-cycling LIBs with temperature adaptability.

Declaration of competing interest

The authors declare that they have no known competing financial interests or personal relationships that could have appeared to influence the work reported in this paper.

Acknowledgments

The authors thank the valuable discussion with Dr. Zhenxing Wang at Jihua Lab. The authors gratefully acknowledge the financial support from the National Natural Science Foundation of China (51972156, 52072378, 52102054 and 51927803), the National Key R&D Program of China (2022YFB3803400, 2021YFB3800301), the Shenyang Science and Technology Program (22-322-3-19), the Youth Fund of the Education Department of Liaoning Province (LJKQZ20222324), and the Outstanding Youth Fund of University of Science and Technology Liaoning (2023YQ11). The authors thank the help of characterization in-situ XRD at Shenyang Industrial Technology Research Institute of Energy Materials and the XAFS test by Prof. Linjuan Zhang, Jianqiu Zhu, Jian-Qiang Wang at Shanghai Institute of Applied Physics, Chinese Academy of Sciences.

Appendix A. Supplementary material

Supplementary material to this article can be found online at https://doi.org/10.1016/j.jechem.2024.02.064.

References

[1] G. Harper, R. Sommerville, E. Kendrick, L. Driscoll, P. Slater, R. Stolkin, A. Walton, P. Christensen, O. Heidrich, S. Lambert, A. Abbott, K. Ryder, L. Gaines, P. Anderson, Nature 575 (2019) 75–86.
[2] S. Sun, C.-Z. Zhao, H. Yuan, Z.-H. Fu, X. Chen, Y. Lu, Y.-F. Li, J.-K. Hu, J.C. Dong, J.-Q. Huang, M.G. Ouyang, Q. Zhang, Sci. Adv. 8 (2022) eadd5189.
[3] W. Li, E.M. Erickson, A. Manthiram, Nat. Energy 5 (2020) 26–34.
[4] L. Wang, T. Liu, T. Wu, J. Lu, Nature 611 (2022) 61–67.
[5] J. Wang, R. Chen, L. Yang, M. Zan, P. Chen, Y. Li, W. Li, H. Yu, X. Yu, X. Huang, L. Chen, H. Li, Adv. Mater. 34 (2022) 2200655.
[6] W. Li, B. Song, A. Manthiram, Chem Soc. Rev. 46 (2017) 3006–3059.
[7] Y. Shen, X. Zhang, L. Wang, D. Zhang, D. Bao, D. Yin, L. Wang, Y. Cheng, G. Huang, Energy Storage Mater. 56 (2023) 155–164.
[8] Z.X. Wang, L.Q. Li, Z.H. Sun, P. Tang, G.J. Hu, J. Tan, F. Li, Progress in Materials Science 143 (2024) 101247.
[9] Z. Li, X. Huang, J. Liang, J. Qin, R. Wang, J. Cheng, D. Wang, J. Energy Chem. 77 (2023) 461–468.
[10] W. Tang, C. Hu, A. Li, X. Huang, Z. Chen, J. Su, W. Zhang, J. Energy Chem. 90 (2024) 412–422.
[11] H.Y. Asl, Manthiram, Arumugam, Science 39 (2020) 140–141.
[12] Y. Cao, N. Li, K. Yuan, N. Li, W. Zhang, S. Liang, Z. Hou, D. Lei, T. Jin, J.-G. Wang, K. Xie, C. Shen, Energy Storage Mater. 60 (2023) 102851.
[13] G.-T. Park, N.-Y. Park, T.-C. Noh, B. Namkoong, H.-H. Ryu, J.-Y. Shin, T. Beierling, C.S. Yoon, Y.-K. Sun, Energy Environ. Sci. 14 (2021) 5084–5095.
[14] Y. Chu, Y. Mu, L. Zou, Y. Hu, J. Cheng, B. Wu, M. Han, S. Xi, Q. Zhang, L. Zeng, Adv. Mater. 35 (2023) e2212308.
[15] T. Weigel, F. Schipper, E.M. Erickson, F.A. Susai, B. Markovsky, D. Aurbach, ACS Energy Lett. 4 (2019) 508–516.
[16] Y.X. Chixia Tian, Dennis Nordlund, Feng Lin, Jin Liu, Zhihong Sun, Yijin Liu, Marca Doeff, Joule 2 (2018) 464–477.
[17] Y. Ma, J.H. Teo, F. Walther, Y. Ma, R. Zhang, A. Mazilkin, Y. Tang, D. Goonetilleke, J. Janek, M. Bianchini, T. Brezesinski, Adv. Funct. Mater. 32 (2022) 2111829.
[18] X. Ou, T. Liu, W. Zhong, X. Fan, X. Guo, X. Huang, L. Cao, J. Hu, B. Zhang, Y.S. Chu, G. Hu, Z. Lin, M. Dahbi, J. Alami, K. Amine, C. Yang, J. Lu, Nat. Commun 13 (2022) 2319.
[19] G. Li, Z. Zhang, R. Wang, Z. Huang, Z. Zuo, H. Zhou, Electrochim. Acta 212 (2016) 399–407.
[20] Z. Sun, Z. Li, L. Gao, X. Zhao, D. Han, S. Gan, S. Guo, L. Niu, Adv. Energy Mater. 9 (2018) 1802946.
[21] X. Fan, X. Ou, W. Zhao, Y. Liu, B. Zhang, J. Zhang, L. Zou, L. Seidl, Y. Li, G. Hu, C. Battaglia, Y. Yang, Nat. Commun. 12 (2021) 5320.
[22] J. Shen, B. Zhang, W. Huang, X. Li, Z. Xiao, J. Wang, T. Zhou, J. Wen, T. Liu, K. Amine, X. Ou, Adv. Funct. Mater. 33 (2023) 2300081.
[23] G. Li, Z. Huang, Z. Zuo, Z. Zhang, H. Zhou, J. Power Sources 281 (2015) 69–76.
[24] A.O. Kondrakov, H. Geßwein, K. Galdina, L. de Biasi, V. Meded, E.O. Filatova, G. Schumacher, W. Wenzel, P. Hartmann, T. Brezesinski, J. Janek, J. Phys. Chem. C 121 (2017) 24381–24388.
[25] L. Ni, H. Chen, W. Deng, B. Wang, J. Chen, Y. Mei, G. Zou, H. Hou, R. Guo, J. Xie, X. Ji, Adv. Energy Mater. 12 (2022) 2103757.
[26] W. Lee, S. Muhammad, T. Kim, H. Kim, E. Lee, M. Jeong, S. Son, J.H. Ryou, W.S. Yoon, Adv. Energy Mater. 8 (2017) 1701788.
[27] S. Mou, K. Huang, M. Guan, X. Ma, J.s. Chen, Y. Xiang, X. Zhang, J. Power Sources 505 (2021) 230067.
[28] C. Ghanty, B. Markovsky, E.M. Erickson, M. Talianker, O. Haik, Y. Tal-Yossef, A. Mor, D. Aurbach, J. Lampert, A. Volkov, J.-Y. Shin, A. Garsuch, F.F. Chesneau, C. Erk, ChemElectroChem 2 (2015) 1479–1486.
[29] A. Gao, Y. Sun, Q. Zhang, J. Zheng, X. Lu, J. Mate. Chem. A 8 (2020) 6337–6348.
[30] J. Li, W. Zhong, Q. Deng, Q. Zhang, Z. Lin, C. Yang, Adv. Funct. Mater. 33 (2023) 2300127.
[31] S. Sun, Z. Han, W. Liu, Q. Xia, L. Xue, X. Lei, T. Zhai, D. Su, H. Xia, Nat Commun 14 (2023) 6662.
[32] C. Geng, D. Rathore, D. Heino, N. Zhang, I. Hamam, N. Zaker, G.A. Botton, R. Omessi, N. Phattharasupakun, T. Bond, C. Yang, J.R. Dahn, Adv. Energy Mater. 12 (2021) 2103067.
[33] C.-S.-Y.-S.-U. Woo, K. Amine, I. Belharouak, Y.-K. Sun, J. Electrochem. Soc. 154 (2007) A1005.
[34] J. Li, J. Harlow, N. Stakheiko, N. Zhang, J. Paulsen, J. Dahn, J. Electrochem. Soc. 165 (2018) A2682–A2695.
[35] Y.G. Zou, H. Mao, X.H. Meng, Y.H. Du, H. Sheng, X. Yu, J.L. Shi, Y.G. Guo, Angew Chem. Int. Ed. Engl. 60 (2021) 26535–26539.
[36] D.S. Ko, J.H. Park, B.Y. Yu, D. Ahn, K. Kim, H.N. Han, W.S. Jeon, C. Jung, A. Manthiram, Adv. Energy Mater. 10 (2020) 2001035.
[37] X.-Y. Hou, Y. Kimura, Y. Tamenori, K. Nitta, H. Yamagishi, K. Amezawa, T. Nakamura, ACS Energy Lett. 7 (2022) 1687–1693.
[38] S. Jamil, M. Fasehullah, B. Jabar, P. Liu, M.K. Aslam, Y. Zhang, S. Bao, M. Xu, Nano Energy 94 (2022) 106961.
[39] F. Wu, N. Liu, L. Chen, Y. Su, G. Tan, L. Bao, Q. Zhang, Y. Lu, J. Wang, S. Chen, J. Tan, Nano Energy 59 (2019) 50–57.
[40] M. Dixit, M. Kosa, O.S. Lavi, B. Markovsky, D. Aurbach, D.T. Major, Phys. Chem. Chem. Phys. 18 (2016) 6799–6812.
[41] T. Zhou, Y. Zhao, M. El Kazzi, J.W. Choi, A. Coskun, Angew. Chem. Int. Ed. Engl. 61 (2022) e202115884.
[42] S. Zhao, Z. Guo, K. Yan, S. Wan, F. He, B. Sun, G. Wang, Energy Storage Mater. 34 (2021) 716–734.
[43] C. Cui, X. Fan, X. Zhou, J. Chen, Q. Wang, L. Ma, C. Yang, E. Hu, X.Q. Yang, C. Wang, J. Am. Chem. Soc. 142 (2020) 8918–8927.
[44] Z. Wang, F. Qi, L. Yin, Y. Shi, C. Sun, B. An, H.M. Cheng, F. Li, Adv. Energy Mater. 10 (2020) 1903843.
[45] C. Yan, X.B. Cheng, Y. Tian, X. Chen, X.Q. Zhang, W.J. Li, J.Q. Huang, Q. Zhang, Adv. Mater. 30 (2018) e1707629.
[46] J.-Y. Hwang, S.-J. Park, C.S. Yoon, Y.-K. Sun, Energy Environ. Sci. 12 (2019) 2174–2184.
[47] D. Wu, J. He, J. Liu, M. Wu, S. Qi, H. Wang, J. Huang, F. Li, D. Tang, J. Ma, Adv. Energy Mater. 12 (2022) 2200337.
[48] G. Hu, Y. Tao, Y. Lu, J. Fan, L. Li, J. Xia, Y. Huang, Z. Zhang, H. Su, Y. Cao, ChemElectroChem 6 (2019) 4773–4780.
[49] Z. Piao, P. Xiao, R. Luo, J. Ma, R. Gao, C. Li, J. Tan, K. Yu, G. Zhou, H.M. Cheng, Adv. Mater. 34 (2022) e2108400.